

**Interreg**  
**Sudoe**



**Samt**  **Sudoe**

European Regional Development Fund



**EFFECT OF PRINTING CONDITIONS ON POROSITY  
FORMATION IN POWDER BED MELTING OF TI-6AL-4V  
PARTS : AN APPROACH BASED ON 3D X-RAY  
TOMOGRAPHY**

## 1- INTRODUCTION

Selective Laser Melting (SLM) is an additive manufacturing process based on powder bed melting and widely studied in recent years for the production of titanium parts (1). A three-dimensional component is built by selectively melting powders within and between layers. The heat source is a finely focused laser and many different metallic powders can be used including aluminum alloys, steels and titanium alloys (2-4). This technology, of considerable importance due its potentially cost effectiveness, low material waste and possibilities it offers to produce complex-shapes components meets a growing success in the aerospace industry. In particular, the Ti-6wt%Al-4wt%V alloy is of interest owing to its high corrosion resistance, and high specific strength. However, actual knowledge on the SLM process remains insufficient and hinders its development on a larger scale (5).

Among the possible reasons, the control of properties of manufactured products is made difficult since it depends on many complex interactions between the input powders, the process and microstructural parameters, the metallurgical defects and the mechanical properties (6). In that context and although SLM of Ti-6Al-4V have made significant advances in the process optimization, built materials are often subject to inner defects or local irregularities which influence their properties. Their role upon mechanical properties was clearly demonstrated. In attendance of porosity, the ultimate tensile strength, elongation and young's modulus were shown to be deteriorated (7). The anisotropy of tensile properties can also be attributed to the orientation of defects with respect to the loading direction (8).



**Figure 1:** A tomography device similar to a medical use for porosity analysis.

If defects are perpendicular to the loading direction, they are expected to open up at relatively low stress levels. Otherwise, if they are parallel to the tensile loading axis, their opening becomes more difficult. Furthermore, the presence of porosity was shown to influence both fracture and fatigue properties. It was observed that cracks initiate from porosity in the substructure and propagate radially outwards (9). Regarding the mechanisms of porosity formation, several sources of porosities were identified i.e. (1) un-melted or partially melted powder particles (2) lack of fusion (3) delamination between adjacent passes or previous deposited layers (4) entrapment of gases during manufacturing. Porosity is usually correlated to the process parameter “energy density” defined by the ratio of laser power (P) to scanning velocity (v), hatch spacing (h) and layer thickness (l) (10, 11):

$$E_v = \frac{P}{v.l.h}, [\text{J/mm}^3] \quad (1)$$

While imperfect, the use of volume energy is certainly the most established approach to control the process/porosity relationship. Indeed, an increase of porosity due to keyholing is expected at high energy density (high laser power and low scan rate), while an increase of porosity due to incomplete melting or “lack of fusion” is expected at lower energy density (low laser power and high speed) and a minimum of porosity is expected at intermediate energy density. The approach based on volume energy presents several major limitations. First, at a given volume energy, this approach fails to capture the effects of printing conditions on porosity formation. Second, it fails to quantify porosity which is formed. In this study, the effect of process parameters on porosity formation was conducted from the measurements by 3D X-Ray tomography of both volume density and volume fraction of pores as a function of the volume energy density (E), the laser power (P) and the scanning velocity

Second, it fails to quantify porosity which is formed. In this study, the effect of process parameters on porosity formation was conducted from the measurements by 3D X-Ray tomography of both volume density and volume fraction of pores as a function of the volume energy density (E), the laser power (P) and the scanning velocity (V), at constant hatch spacing (h) and layer thickness (l). The results obtained were analyzed and rationalized from a simple theoretical approach.

## 2-MATERIALS, PRINTING CONDITIONS AND METHODS

### 2.1 Ti-6Al-4V INPUT POWDER

Titanium Ti-6Al-4V (Ti - 6wt% Al - 4wt% V) powder feedstock from Tekna and produced by plasma atomization was used in this study. The micrograph obtained by scanning electron microscopy gives an example of the powder characteristics. They have a spherical shape and the median particle size was measured around 11  $\mu\text{m}$ , the D 10 was 7  $\mu\text{m}$  and the D 90 was 17.5  $\mu\text{m}$  (12). The chemical composition of the Ti-6Al-4V powder is given in Table 1.

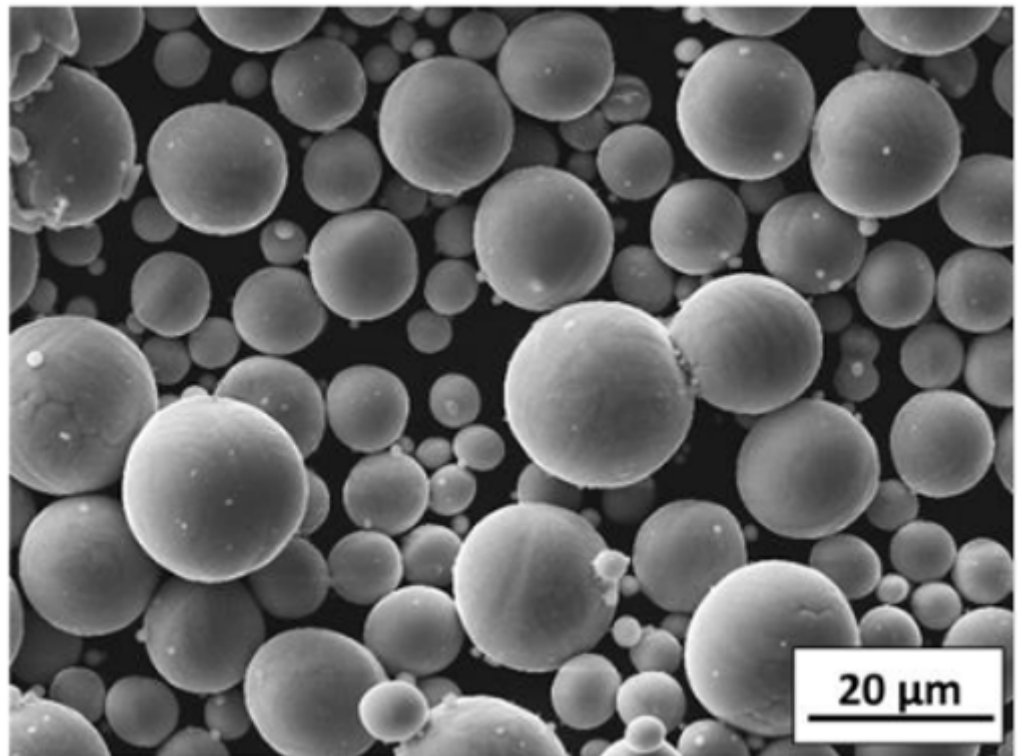
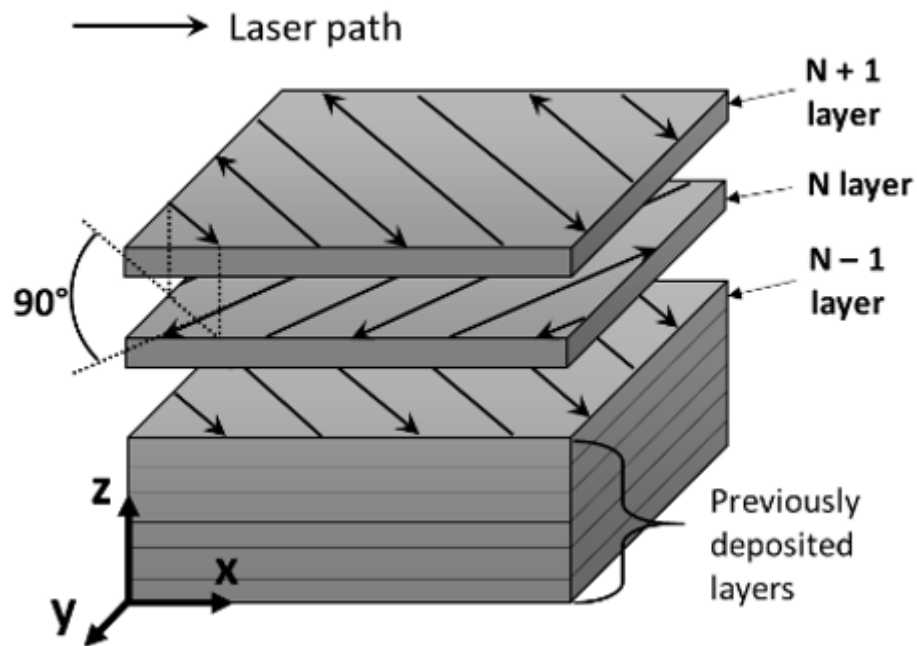


Figure 2 : SEM de Ti-6Al-4V

Table 1: Chemical composition of Ti-6Al-4V powder

Chemical composition in wt. %					
Ti	Al	V	Fe	O	H
bal.	5.77	3.91	0.22	0.12	0.006





**Figure 3:** Schematic representation of the scanning strategy consisting of a pattern of straight lines with a 90-degree rotation between each successive layer. The x, y and y and z axes represent the loading direction of the powder, the roller axis and the stacking direction of the layers, respectively.

## 2. 2.PRINTING CONDITIONS

Parts with a dimension of  $3 \times 3 \times 5 \text{ cm}^3$  were manufactured by selective laser melting of Ti-6Al-4V powders on the ProX 300 from 3D systems. The x, y and z axis represent the powder loading direction, the axis of the roller, and the layer stacking direction respectively (Figure 3). All parts were built in a protective Argon atmosphere and the process parameters studied are summarized in Table 2. The scanning strategy, given in Figure 3, consists of straight lines with a  $90^\circ$  rotation between layers.

Table 2: Laser process parameters studied in this work

Laser power (W)	Laser scanning speed (mm/s)	Hatch spacing ( $\mu\text{m}$ )	Spot size ( $\mu\text{m}$ )	Powder layer thickness ( $\mu\text{m}$ )	Energy density ( $\text{J}/\text{mm}^3$ )	Sample
100	650	50	70	60	51.0	1
250	1625	50	70	60	51.0	2
350	2275	50	70	60	51.0	3
100	450	50	70	60	74.0	4
250	1125	50	70	60	74.0	5
100	220	50	70	60	151.0	6
250	550	50	70	60	151.0	7
350	770	50	70	60	151.0	8

## 2.3 METHODS



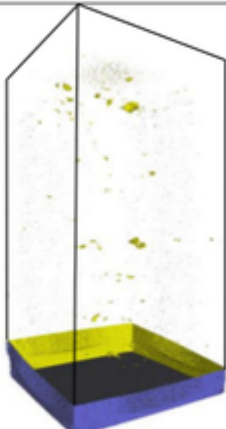
The analysis of the porosity was performed by X-ray micro-computed tomography ( $\mu\text{CT}$ ). A Phoenix Nanotom was used to characterize the 3D distribution and both the volume fraction ( $F_v$ ) and the mean volume ( $\langle V \rangle$ ) of pores. The  $\mu\text{CT}$  equipment was composed of an X-ray nanofocus tube operating up to 180 kV/15W and an X-ray scintillator screen which was coupled to a high-resolution Hamamatsu CCD-sensor (2300 pixels 2300 pixels). The  $\mu\text{CT}$  procedure was based on the acquisition of a series of X-ray radiographs of a sample that rotated step by step around a vertical axis perpendicular to the incident beam. Images were recorded over a period of 750 ms 6 times for each one, to obtain an average one, with a step of 0.36. An energy of 100 keV was used for the tomographic scans. For 3D-imaging reconstruction, a mathematical algorithm was used to reconstruct the distribution of absorption coefficients within the sample volume, and then, the internal 3D volume structure of the samples. The final resolution of the 3D-images was voxels of dimensions  $2\text{ }\mu\text{m} \times 2\text{ }\mu\text{m} \times 2\text{ }\mu\text{m}$ . Specimens with  $2 \times 1 \times 10\text{ mm}^3$  dimensions were removed from the as-built sample.

### 3. RESULTS AND DISCUSSION

#### 3.1. ANALYSIS OF THE POROSITY FORMATION AS A FUNCTION OF PRINTING CONDITIONS

The 3D  $\mu$ CT views of pores in the as-built sample as a function of process parameters are given in Figure 3. Voids are represented in yellow. The x, y and z-dimensions of the represented volume are respectively 2 mm, 1 mm and 10 mm. The smallest observable size of voids is limited by the  $\mu$ CT spatial resolution of 2  $\mu$ m. In this representation, no particular arrangement of voids can be seen. The volume fraction and the mean volume of pores volume vary between (0.03 – 9.78) and ( $5.0 \times 10^{-3} \text{ mm}^3$  –  $1.1 \text{ mm}^3$ ) respectively as a function of printing conditions.

For the same energy density, both the volume fraction and the mean volume of pores decrease as laser power increases and laser scanning speed decreases. The densest part was obtained the energy density of  $74 \text{ J/mm}^3$  for the particular set of parameters of 250W and 1125 mm/s as power laser and laser scanning speed, respectively (sample 5). A very interesting thing is that the morphology of pores depends on the printing conditions. For the highest energy density ( $151 \text{ J/mm}^3$ ), they have a near spherical morphology while they have a more elongated morphology for the energy density of  $51 \text{ J/mm}^3$ . The situation is however somewhat more nuanced at  $74 \text{ J/mm}^3$  where the morphology of pores is, elongated for a laser power and a laser scanning of 100W and 450mm/s, respectively (sample 4) and spherical for a laser power and a laser scanning of 250W and 1125 mm/s, respectively (sample 5). This is a key point since the mechanism of porosity formation is generally related to their morphology (13).

	1	2	3
	$F_v=9.78$ $\langle V \rangle=1.1 \text{ mm}^3$	$F_v=0.13$ $\langle V \rangle=2 \times 10^{-2} \text{ mm}^3$	$F_v=0.06$ $\langle V \rangle=9 \times 10^{-3} \text{ mm}^3$
$E_v=51 \text{ J/mm}^3$			
	4	5	
	$F_v=0.88$ $\langle V \rangle=1.3 \times 10^{-1} \text{ mm}^3$	$F_v=0.03$ $\langle V \rangle=5.0 \times 10^{-3} \text{ mm}^3$	

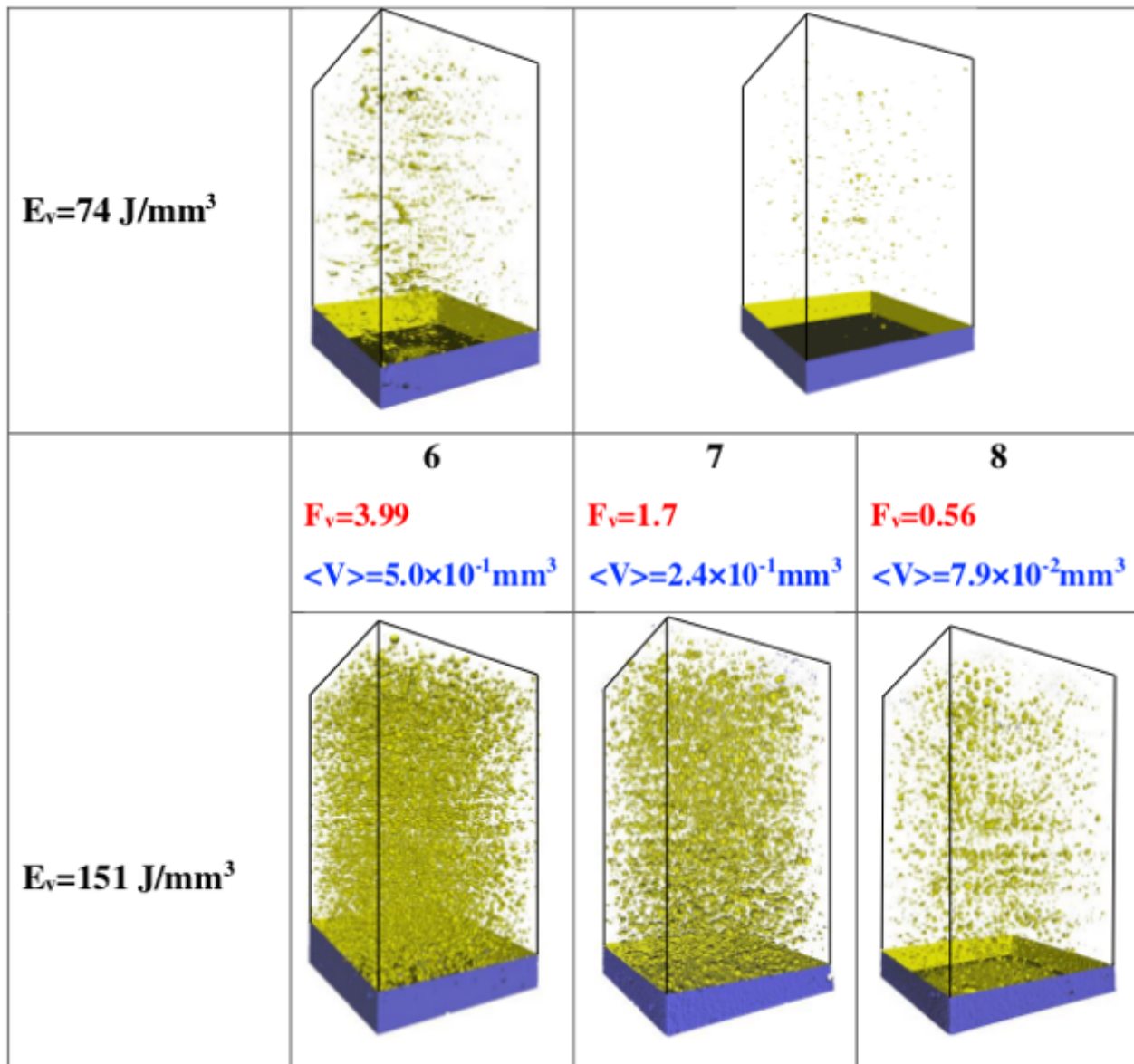


**Figure 4:** Three-dimensional  $\mu$ CT view of porosity as a function of printing conditions. The printing conditions corresponding to the samples from 1 to 8 are given in table 2.  $F_v$  and  $\langle V \rangle$  correspond to the volume fraction and mean volume of pores.

The overall experimental results can be displayed in an original 2D diagram (Figure 5) which give a better appreciation of the effects of printing conditions on the porosity formation. Contrary to what it is often claimed in the literature, it becomes clear that the porosity evolves significantly for the same density energy. For instance, it can be orders of magnitude at  $51 \text{ J/mm}^3$  and  $74 \text{ J/mm}^3$ . Furthermore, two similar porosity state can be obtained for two different density energy.



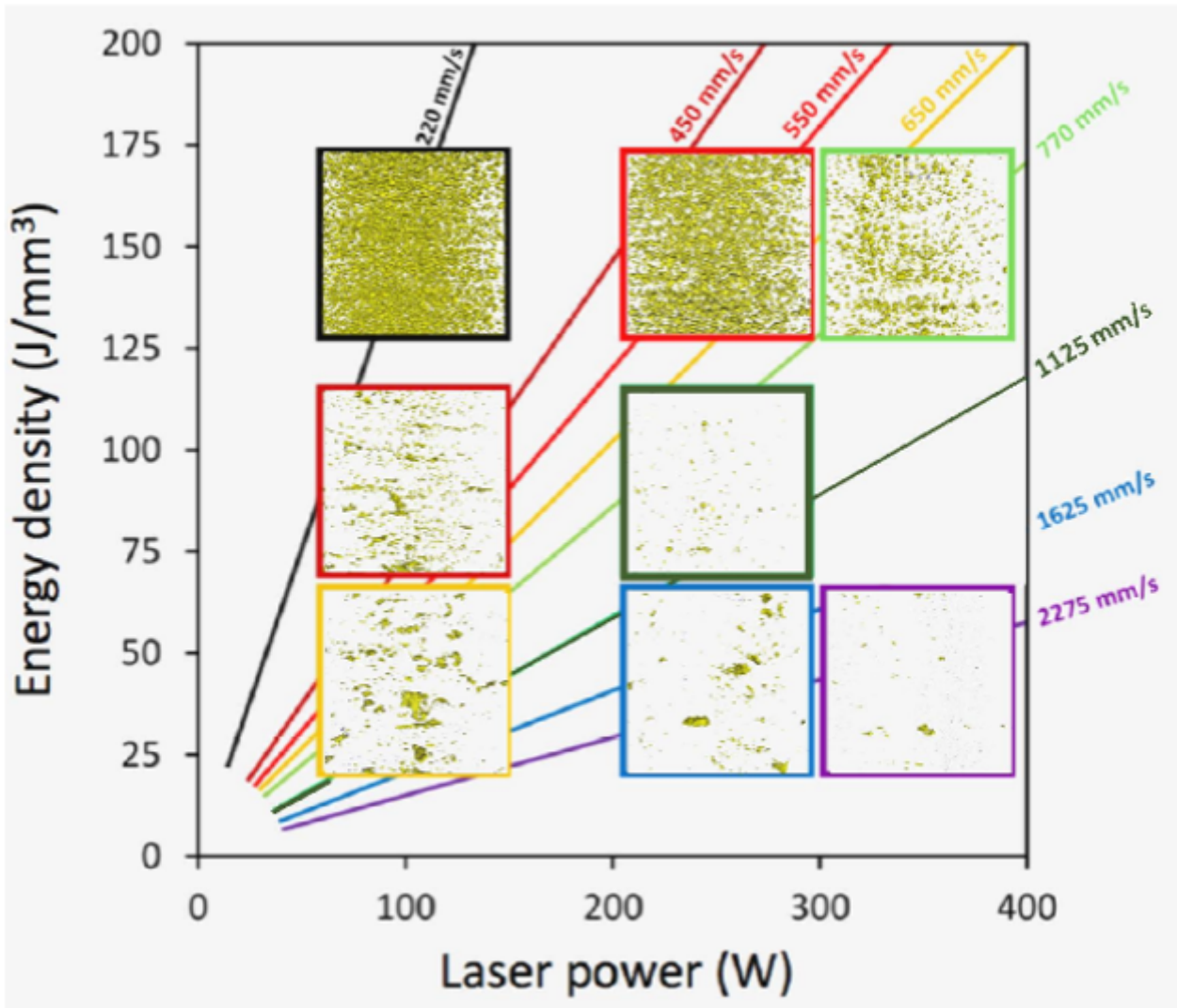


**Figure 5:** 2D diagram of the evolution of the porosity state as a function of energy density, laser power and laser scanning speed.

### 3.1 RATIONALIZATION FROM A THEORETICAL APPROACH

The fundamental origin of lack-of-fusion porosity is insufficient overlap of successive melt pools. In the approach present here, melt-pool overlap is calculated to predict lack-of-fusion porosity. The fundamental principle behind calculation is that, for complete melting, the depth of the overlap between laterally adjacent melt pools  $L^*$  must be at least as large as the layer thickness  $t$  used for part printing (see Figure 6). In the following, a semi-circular melt pool cross sectional shape was considered. From geometrical considerations, it can be easily shown that:

$$\left(\frac{h}{2}\right)^2 + (L^*)^2 = \left(\frac{W}{2}\right)^2$$

The necessary and sufficient condition for width and depth overlapping is that  $L^* = t$ . In that case, the lack of fusion takes place if the following relation is verified:

$$\left(\frac{h}{W}\right)^2 + \left(\frac{t}{D}\right)^2 \geq 1 \quad (1)$$

where,

$$D = \frac{W}{2}$$

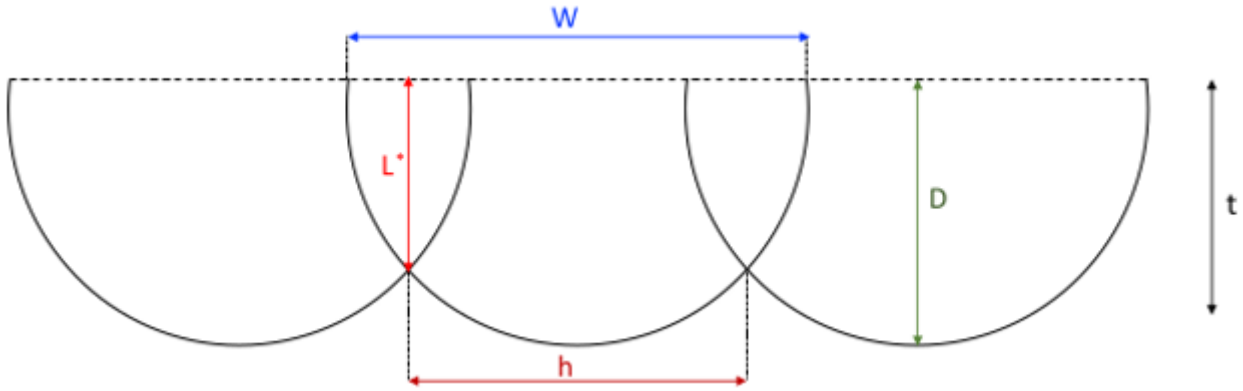


**Figure 6:** Schematic representation of the assumed semi-circular shape of melt pools.  $W$ ,  $h$ ,  $D$ ,  $t$  and  $L^*$  represent the melt-pool width, the hatch spacing, the melt pool depth, the layer thickness and the depth of the overlap between laterally adjacent melt pools.

The second step of our approach is to determine the melt pool size as a function of printing conditions. The melt-pool size depends primarily on absorbed power, beam speed and the thermal properties (conductivity and diffusivity) of the materials and can be determined from the simple analytical Rosenthal equation that gives the evolution of the thermal profile for a heat source of speed  $V$  (14). It relies on the following assumptions: only conduction is considered, heat of fusion is not included and the properties do not depend on temperature. These assumption were recently validated from 3D numerical calculations (15). From the thermal profile calculated from the Rosenthal, it is possible to show that the width of the melt pool can be approximated by (16) :

$$W \approx \sqrt{\frac{8\lambda P}{2.7\pi\rho C_p V(T_f - T_0)}} \quad (2)$$

where  $\lambda$  is absorptivity,  $\rho$  is density,  $C_p$  is specific heat and  $T_f$  is the melting temperature. The process parameter “energy density”  $E_v$  is defined by the ratio of laser power ( $P$ ) to scanning velocity ( $V$ ), hatch spacing ( $h$ ) and layer thickness ( $t$ ) :

$$h = \frac{P}{E_v \cdot t \cdot V}$$

by taking into account the relation (2), the following relation can thus be obtained

$$\frac{h}{W} = \frac{\frac{2.7\pi\rho C_p (T_f - T_0)}{4E_v \lambda}}{\left(\frac{t}{D}\right)} \quad (3)$$

In a diagram  $\frac{h}{W} = f\left(\frac{e}{D}\right)$  the conditions for porosity formation by lack-of-fusion can be represented by a quarter circle (see relation (1)). On this same diagram and from relation (3), the evolution of  $\frac{h}{W}$  as a function of  $\frac{t}{D}$  can be plotted for both a given energy density and absorptivity. The experimental data can also be represented on the curve  $\frac{h}{W} = f\left(\frac{e}{D}\right)$  if one take into account that  $2W=D$ . Indeed, in that case, the relation (3) leads to:

$$\frac{h}{W} = \frac{\sqrt{h} \sqrt{\frac{2.7\pi\rho C_p (T_f - T_0)}{4\lambda}}}{\sqrt{2E_v t}} \quad (4)$$

the experimental data are thus located on the corresponding iso-energy density  $E_v$  with an ordinate  $h/W$  that depends on printing conditions. While the absorptivity is expected to be affected by other factors such as processing parameters ( $P$  and  $V$ ) and melt-pool surface roughness, it was assumed, for sake of simplicity, constant. The thermo-physical data used for calculations are summarized in Table 3 and the main results obtained are given in Figure 8.

The analysis of the results (Figure 7) leads to the following conclusions. At a given energy density and depending on the printing conditions, the parts printed can either be free of porosity or to contain porosity formed by incomplete melting or overmelting. The implication is that an increase in energy density does not necessarily improve part density, and that maintaining a constant energy density (while changing other processing conditions) may result in varying porosity. As a consequence, the “energy density” parameter is not completely relevant for controlling the relationship between the printing conditions and porosity formation. Furthermore, there is a critical energy density of  $40 \text{ J/mm}^3$  below which the formation of porosity by incomplete melting can not be prevented.

**Table 3: Thermo-physical data used for calculation (16)**

QUANTITY	VALUE
Melting temperature	1913 K
Density $\rho$	$4430 \text{ kg/m}^3$
Specific heat $C_p$	$526 \text{ J/kg/K}$
Absorptivity $\lambda$	0.40

At iso-density energy, the experimental points coincide on Figure 8 for the reason that layer thickness and hatch spacing are the same for all the printing conditions and absorptivity is assumed constant and thus independent on printing parameters such as laser power and laser scan speed. At high energy density of  $151 \text{ J/mm}^3$ , it is shown that pores are formed by overmelting while at lower energy density ( $51 \text{ J/mm}^3$ ), it is shown that pores are formed by incomplete melting. It is very consistent with the porosity morphology observed. Indeed, near spherical pores are associated to an excessive energy density while those elongated are associated to a lack of fusion (17, 18). The parametric study (Figure 7) shows that hatch spacing has a significant effect on both the mechanism of porosity formation and the quantity of porosity which is formed. Surprisingly, this effect is all the more important the energy density is low. The approach proposed can be used as a guideline to design TA6V part by selective laser melting.

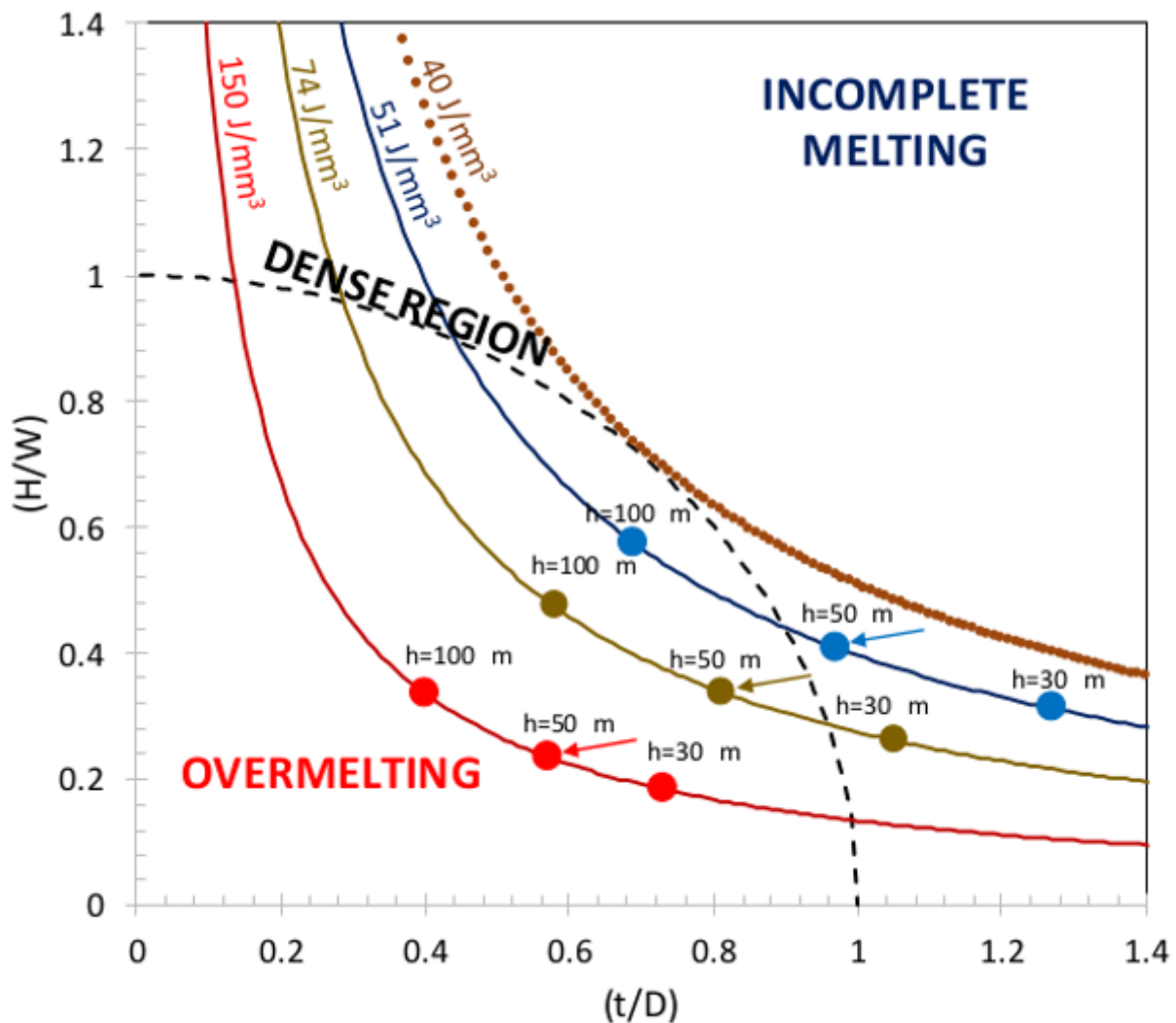


**Figure 7 :**  $\frac{h}{W} = f\left(\frac{t}{D}\right)$  diagram. The position of experimental data are indicated by arrows. The quarter circle defined by  $\frac{h}{W}=1$  and  $\frac{t}{D}=1$  give the overmelting, dense and incomplete melting zones. The iso-density lines show that the 'energy density' parameter is not necessarily relevant for controlling the relationship between the printing conditions and porosity formation.

## REFERENCES

- (1) L.-C. Zhang, H. Attar, Selective Laser Melting of Titanium Alloys and Titanium Matrix Composites for Biomedical Applications: A Review , *Adv. Eng. Mater.* 18 (2016) 463–475
- (2) E.O. Olakanmi, R.F. Cochrane, K.W. Dalgarno, A review on selective laser sintering/melting (SLS/SLM) of aluminium alloy powders: Processing, microstructure, and properties, *Prog. Mater. Sci.* 74 (2015) 401–477
- (3) H. Schwab, F. Palm, U. Kühn, J. Eckert, Microstructure and mechanical properties of the near-beta titanium alloy Ti-5553 processed by selective laser melting, *Mater. Des.* 105 (2016) 75–80
- (4) M. Akita, Y. Uematsu, T. Kakiuchi, M. Nakajima, R. Kawaguchi, Defect-dominated fatigue behavior in type 630 stainless steel fabricated by selective laser melting, *Mater. Sci. Eng. A.* 666 (2016) 19–26
- (5) W.E. Frazier, Metal additive manufacturing: A review, *J. Mater. Eng. Perform.* 23 (2014) 1917–1928
- (6) M. Simonelli, Y.Y. Tse, C. Tuck, Microstructure of Ti-6Al-4V produced by selective laser melting, *J. Phys. Conf. Ser.* 371 (2012)
- (7) H. Gong, K. Rafi, H. Gu, G.D. Janaki Ram, T. Starr, B. Stucker, Influence of defects on mechanical properties of Ti-6Al-4V components produced by selective laser melting and electron beam melting, *Mater. Des.* 86 (2015) 545–554
- (8) T. Vilaro, C. Colin, J.D. Bartout, As-fabricated and heat-treated microstructures of the Ti-6Al-4V alloy processed by selective laser melting, *Metall. Mater. Trans. A Phys. Metall. Mater. Sci.* 42 (2011) 3190–3199
- (9) H. Gong, K. Rafi, H. Gu, G.D. Janaki Ram, T. Starr, B. Stucker, Influence of defects on mechanical properties of Ti-6Al-4V components produced by selective laser melting and electron beam melting, *Mater. Des.* 86 (2015) 545–554
- (10) L. Thijs, F. Verhaeghe, T. Craeghs, J. Van Humbeeck, J.P. Kruth, A study of the microstructural evolution during selective laser melting of Ti-6Al-4V, *Acta Mater.* 58 (2010) 3303–3312
- (11) M. Simonelli, Y.Y. Tse, C. Tuck, Microstructure of Ti-6Al-4V produced by selective laser melting, *J. Phys. Conf. Ser.* 371 (2012)
- (12) J. Stef, Thèse de Doctorat de l'Université de Bordeaux, 2018
- (13) H. Gong, K. Rafi, H. Gu, T. Starr, B. Stucker, Analysis of defect generation in Ti-6Al-4V parts made using powder bed fusion additive manufacturing processes, *Addit. Manuf.* 1 (2014) 87–98
- (14) D. Rosenthal, Mathematical theory of heat distribution during welding and cutting, *Weld Journal* 20(5) 1941 220–234
- (15) P. Promoppatum, S-C Yao, P. C. Pistorius, A. D. Rollet, *Engineering* 3 (2017) 685–694
- (16) M. Tang, P. C. Pistorius, J. L. Beuth, *Additive Manufacturing* 14 (2017) 39–48
- (17) H. Gong, H.K. Rafi, N. V Karthik, T.L. Starr, B.E. Stucker, Defect morphology in Ti-6Al-4V parts fabricated by selective laser melting and electron beam melting, *Solid Free. Fabr. Symp. Symporisum Proceeding.* (2013) 440–453
- (18) J. Stef J., A. Poulon-Quintin, A. Redjaimia A, J. Ghanbaja, O. Ferry, M. De Sousa, M. Gouné, Mechanism of porosity formation and influence on mechanical properties in selective laser melting of Ti-6Al-4V parts. *Materials & Design* 2018, vol. 156, p. 480–493





The Interreg Sudoe programme is financed by the European Regional Development Fund (FEDER).